JOURNAL OF SYNCHROTRON RADIATION

ISSN 1600-5775

High-efficiency fast X-ray imaging detector development at SSRF

Honglan Xie,[a,b]* Hongxin Luo,[a,b] Guohao Du,[a,b] Chengqiang Zhao,[c] Wendong Xu,[c] Guangzhao Zhou,[a,b] Rongchang Chen[a,b] and Tiqiao Xiao[a,b]

[a]Shanghai Synchrotron Radiation Facility (SSRF), Shanghai Institute of Applied Physics, Chinese Academy of Sciences, Shanghai, People's Republic of China, [b]Shanghai Advanced Research Institute, Chinese Academy of Sciences, Shanghai, People's Republic of China, and [c]Shanghai Institute of Optics and Fine Mechanics, Chinese Academy of Sciences, Shanghai, People's Republic of China. *Correspondence e-mail: xiehonglan@sinap.ac.cn

Received 26 September 2018
Accepted 14 July 2019

Edited by A. Momose, Tohoku University, Japan

Keywords: scintillators; indirect X-ray imaging detectors; long-working-distance microscope lenses; fast X-ray imaging; fast X-ray microtomography; CMOS cameras; dynamic X-ray micro-CT; synchrotron radiation.

Supporting information: this article has supporting information at journals.iucr.org/s

Indirect X-ray imaging detectors consisting of scintillator screens, long-working-distance microscope lenses and scientific high-speed complementary metal-oxide semiconductor (CMOS) cameras are usually used to realize fast X-ray imaging with white-beam synchrotron radiation. However, the detector efficiency is limited by the coupling efficiency of the long-working-distance microscope lenses, which is only about 5%. A long-working-distance microscope lenses system with a large numerical aperture (NA) is designed to increase the coupling efficiency. It offers an NA of 0.5 at 8× magnification. The Mitutoyo long-working-distance microscope lenses system offers an NA of 0.21 at 7.5× magnification. Compared with the Mitutoyo system, the developed long-working-distance microscope lenses system offers about twice the NA and four times the coupling efficiency. In the indirect X-ray imaging detector, a 50 µm-thick LuAG:Ce scintillator matching with the NA, and a high-speed visible-light CMOS FastCAM SAZ Photron camera are used. Test results show that the detector realized fast X-ray imaging with a frame rate of 100000 frames s^{-1} and fast X-ray microtomography with a temporal sampling rate up to 25 Hz (25 tomograms s^{-1}).

1. Introduction

High-speed X-ray imaging is a very important tool in scientific research. As we know, a fundamental and enduring scientific challenge is to understand the relationship between structure and function at the time scales of dynamics processes and then to control their complex dynamic behavior. To understand and control the high-speed processes depends on real-time observations. For example, real-time observation of failure dynamics processes of materials and structures, such as deformation, damage and fracture under strong dynamic load, can contribute to develop new shock-resistance high-strength materials. Also, real-time observation of fuel-spray dynamics processes, such as blasting, crushing and atomization, can contribute to develop new gas engines with higher combustion efficiency and lower carbon emission. Scientists have been developing fast X-ray imaging to observe *in situ* failure dynamics processes of materials and structures under load (Luo *et al.*, 2012; Hudspeth *et al.*, 2013, 2015; Chen, Hudspeth *et al.*, 2014; Fan *et al.*, 2014; Huang *et al.*, 2016; Olbinado *et al.*, 2018), and high-speed fuel-spray processes (MacPhee *et al.*, 2002; Wang, 2005; Fezzaa & Wang, 2008; Wang *et al.*, 2008; Lee *et al.*, 2012; Halls *et al.*, 2017). Moreover, real-time observation of the 3D microstructure evolution of materials with fast X-ray microtomography is also very important in studying the dynamic behavior of materials. Up to now, a fast X-ray

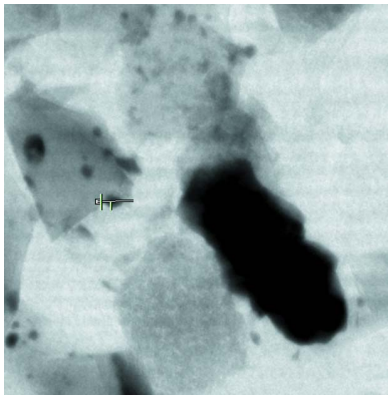

microtomography experiment with a temporal sampling rate up to 25 Hz (25 tomograms s^{-1}) has been realized (García-Moreno *et al.*, 2018).

To realize real-time observation of high-speed processes, a high-speed and high-sensitive X-ray imaging detector is key. X-ray imaging detectors with hard X-rays usually use an indirect detection mode: a fluorescent screen, visible-light optics and a camera (Koch, 1994; Koch *et al.*, 1998; Bonse & Busch, 1996; Rack *et al.*, 2010; Olbinado *et al.*, 2017*a*,*b*; Xie *et al.*, 2013, 2016; Chen, Liu *et al.*, 2014). The visible-light optics has two options: either optical fiber or microscope lenses. The fiber-coupling type detectors have a high efficiency but the spatial resolution is limited by the fiber size. The microscope-lenses-coupling detectors can realize spatial resolution up to submicrometres, which is currently the most popular with the highest-use frequency on X-ray imaging beamlines in the world. Indirect X-ray imaging detectors consisting of scintillator screens, long-working-distance microscope lenses and scientific high-speed complementary metal-oxide semiconductor (CMOS) cameras are usually used to realize fast and high-resolution X-ray imaging with white/pink beam synchrotron radiation. However, the detector efficiency is limited by the coupling efficiency of the long-working-distance microscope lenses, which is only about 5%, and limited by its numerical aperture (NA). The efficiency of the indirect detector with high spatial resolution is decided by the absorption coefficient of the scintillator, and the light-collection efficiency and the quantum efficiency of the sensor of the corresponding camera (Koch *et al.*, 1998). However, frequently the stopping power of a thin scintillator used for high resolution down to micrometre/submicrometre X-ray imaging is very limited, and the NA of the long-working-distance microscope lenses is low and limits the light-collection efficiency.

In order to realize fast X-ray imaging with high spatial resolution at the Shanghai Synchrotron Radiation Facility (SSRF), a fast X-ray imaging detector based on a long-working-distance microscope lenses system with a large NA and a CMOS-based digital high-speed camera was developed. By optimizing the optical path of the optical microscope coupling system of the detector, we enlarged the NA of the microscope objective and reduced the radiation damage on it substantially, so as to improve the light-collection efficiency and light-transmission efficiency of the detector. The performance of several kinds of scintillator materials and the effect of scintillator thickness on the performance of the X-ray imaging detector was studied to further improve the efficiency of the detector. This article will report test results of the developed fast X-ray imaging detector. The test results show that the detector realized fast X-ray imaging with a frame rate of 100000 frames s^{-1} and fast micro-computed tomography (micro-CT) with a temporal sampling rate up to 25 Hz.

2. Design scheme

Fast X-ray imaging detectors in indirect detection mode use fast-response scintillators to convert X-rays into visible light and then are coupled to high-speed visible-light CMOS cameras through optical microscope systems.

The high-resolution fast X-ray imaging indirect detectors use optical microscope objective coupling to realize micrometre, even submicrometre, spatial resolution. A microscope objective is usually placed close to the scintillator to reach a large NA of the microscope objective. However, the microscope objective is noticeably blackened by radiation damage from the high-brightness synchrotron radiation, and the light-transmission efficiency is reduced considerably. Therefore, the original intention of improving the detector efficiency by using a large NA of the microscope objective placed close to the scintillator has not been realized.

The optical microscope objective coupling system of the developed fast X-ray imaging detector in this article adopts an L-shape optical path with a long working distance, and the microscope objective is placed behind the reflecting mirror (Koch, 1994; Douissard *et al.*, 2012). Therefore, the microscope objective is not in the direct X-ray path and is protected from radiation damage caused by direct X-rays.

The design scheme, shown in Fig. 1, consists of a scintillator, a reflect mirror, a microscope objective and a high-speed CMOS camera.

The main design points are as follows.

(1) An L-shape optical path is used, in which the microscope objective is placed behind the mirror to avoid being exposed in the direct high-intensity X-ray path. A piece of lead glass is placed in front of the microscope objective, which significantly reduces the radiation damage of the microscope objective and improves the light-transmission efficiency.

(2) The optical microscope objective coupling system is designed optimally to realize a large NA microscope objective, which can greatly improve the light-collection efficiency.

(3) The scintillator thickness is matched optimally with the NA of the microscope objective to realize optimal imaging resolution and optimal imaging contrast.

(4) The scintillator with high luminescence efficiency, short afterglow and radiation resistance is used to improve the efficiency of X-rays converted into visible light.

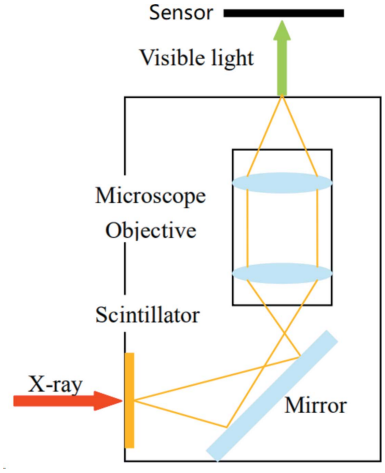

Figure 1
Sketch of the indirect detector system.

(5) An ultrathin metal reflection film is coated on the incident surface of the scintillator to prevent the dust of electrostatic adsorption from being imaged. An ultrathin anti-reflection film is coated on the exit surface of the scintillator to increase the transmittance of the visible light.

As a high-speed visible-light CMOS camera, a FastCAM SAZ camera from Photron (Photron Co., Tokyo, Japan) is used (Manin *et al.*, 2018). The pixel size is 20 µm, the dynamic range is 12 bit and the memory is 64 GB. In the case of 640 × 280 pixel resolution, the maximum frame rate is up to 100000 frames s^{-1}. According to the development target of the fast X-ray imaging detector of 100000 frames s^{-1} and a beam size of 1.6 mm by 0.7 mm at the position of the sample, the optimal magnification of the microscope objective is 8 and the effective pixel size is 2.5 µm. The size of the corresponding field of view is 1.6 mm by 0.7 mm, perfectly matched with the beam size at the position of the sample.

3. Optical design of a large-NA optical coupling system

The optical coupling efficiency g_2 of the lenses system, purely from solid-angle considerations, is given by (Yeom *et al.*, 2010)

$$g_2 = \tau\left[\frac{M}{2F(1+M)}\right]^2, \qquad (1)$$

where τ is the transmission efficiency of optical photons through all the glass lenses, M is the magnification of the lenses, and F is the ratio of the focal length to the lenses diameter and equals 1/(2NA).

According to equation (1), the larger the NA of the lenses, the higher the optical coupling efficiency of the lenses. For low-dose imaging, in order to enlarge the NA as much as possible, the lenses are placed close to the scintillator. For high-dose imaging, in order to avoid radiation damage of the lenses by a high-energy beam with high heat load, the microscope objective is placed behind the mirror. Thus, compared with the low-dose microscopic coupling system, the high-dose microscopic coupling system has a longer working distance, a smaller NA and a lower coupling efficiency. The parameters of long-working-distance lenses from Mitutoyo (Mitutoyo Co. Ltd, Kawasaki, Japan) and self-developed ones are shown in Table 1. Parameters for the long-working-distance lenses from Mitutoyo can also be found elsewhere (Douissard *et al.*, 2012).

According to Table 1 and equation (1), the optical coupling efficiency of the high-dose optical coupling system is about 5%, which is proportional to the square of the NA of the optical coupling system and affects the temporal resolution of high-dose X-ray imaging. Therefore, we optimized the optical design of the coupling system to increase the NA and hence improve the coupling efficiency. The development goal of the optical coupling system is to increase its NA to 0.5 at 8× magnification, and then its coupling efficiency is improved to 17%, which is about five times the coupling efficiency of the commercial coupling system which has a NA of 0.21 at 7.5× magnification. Up to now, a new Mitutoyo long-working-distance objective has been available with a larger NA of 0.42 at 10× magnification, meaning its coupling efficiency is improved to 14%. Therefore, enlarging the NA of the long-working-distance objective to improve the detector efficiency is very effective.

Table 1
Comparison of parameters between Mitutoyo long-working-distance lenses and self-developed ones.

	Long-working-distance lenses				
	Mitutoyo				Self-developed
Magnification	2×	5×	7.5×	10×	8×
NA	0.05	0.14	0.21	0.28	0.5
Working distance (mm)	34	34	35	33.5	31.7
Coupling efficiency (%)	0.11	1.3	3.4	6.5	17

The optical beam path of an indirect detection system compatible with high-energy illumination is shown in Fig. 2. A scintillator material of LuAG:Ce with a layer of 100 nm-thick aluminium reflection coating on the scintillator incident surface and a layer of 100 nm-thick anti-reflection coating on the scintillator exit surface was chosen, and an optimal scintillator thickness of 50 µm matching with the NA of 0.5 was used. The scintillator was mounted on a spring base and can easily be replaced. The lead glass is used to absorb scattered X-rays, and its thickness is 4.5 mm [Model ZF7 from CDGM Glass (Chengdu, People's Republic of China)]. The NA is 0.5 and the working distance is 31.7 mm. This large-NA and long-working-distance lenses system is suitable for high-dose high-speed imaging. The maximum object field-of-view of the designed optical system is 1.75 mm and the magnification of

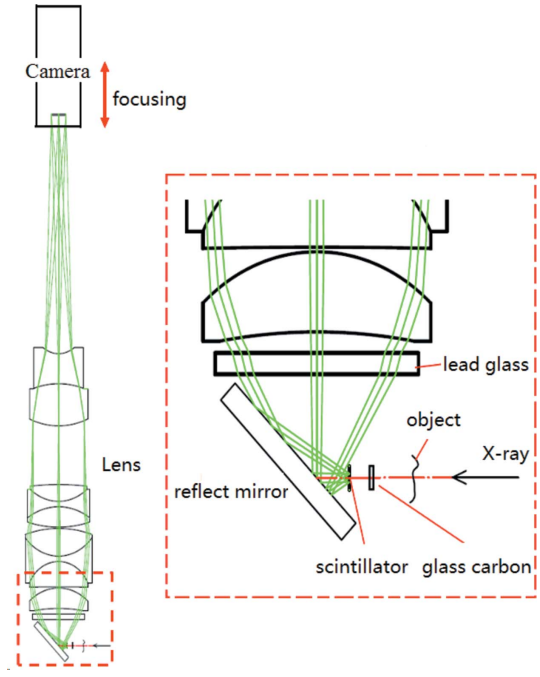

Figure 2
Optical beam path of the indirect detection system compatible with high-energy illumination.

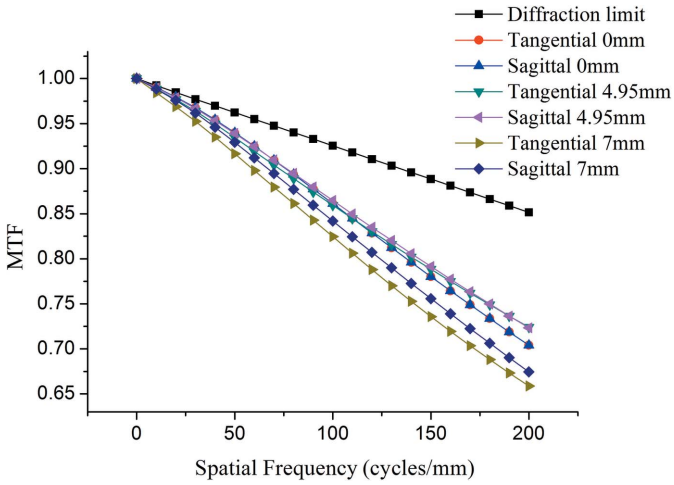

Figure 3
MTF of the high-dose optical coupling system.

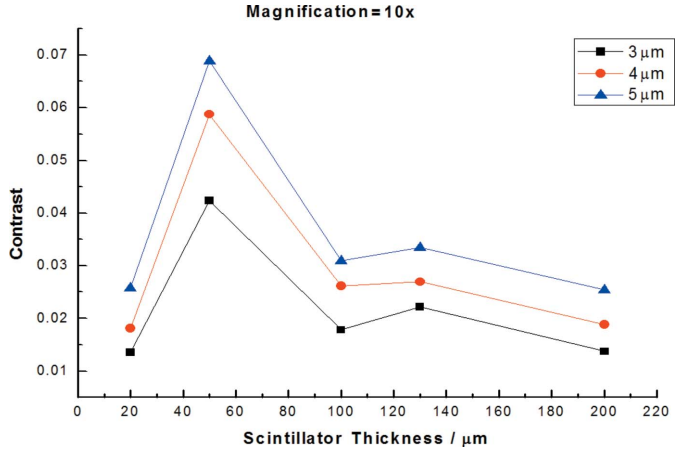

Figure 4
Influence of the scintillator thickness on the contrast of images of differently sized features in the JIMA RT RC-02 test pattern with a 10× lenses system at 18 keV.

the optical system is 8×, so the maximum image field-of-view is 14 mm. The magnification of the lenses system is 8× and the effective pixel size is 2.5 μm. Therefore, the maximum field-of-view of the developed detector is 2.5 mm. The modulation transfer function (MTF) curve of the lenses system is shown in Fig. 3, and shows that the contrast ratio of the lenses system is more than 65%. The CMOS camera is moved up and down to adjust the focus. A gas-cooling structure is designed to protect the scintillator (Zhou *et al.*, 2018). However, considering that gas flow may cause scintillator vibration in our case, the gas-cooling system is not used in the experiments in this article.

4. Thickness optimization of scintillators

The afterglow time of scintillator materials must be considered in addition to the emission wavelength and luminous efficiency of the scintillator materials. For microsecond time-resolved X-ray imaging, the afterglow time is required to be of the order of nanoseconds. Only YAG:Ce (τ = 96 ns), LuAG:Ce (τ = 61 ns) and LYSO:Ce (τ = 41 ns) are available commercially to meet these requirements (Rutherford *et al.*, 2016).

Compared with the YAG:Ce scintillator, the LuAG:Ce scintillator with higher luminous efficiency is selected on the premise that the emission wavelength is matched with the detector and the afterglow time is short.

In general, a thick scintillator has a higher efficiency while the spatial resolution becomes worse when the penetration length of X-ray photons in the scintillator is more than the depth of field of the microscope lenses system; and a thin scintillator has a higher resolution down to submicrometre levels where frequently the stopping power of the scintillator is limiting the efficiency. Therefore, an optimal scintillator thickness should be found. Based on previous experimental studies, we found that matching the scintillator thickness with the NA of the lenses system will significantly improve the imaging contrast (Xie *et al.*, 2016). According to the equation of the spatial resolution of the lenses system which combines diffraction and defect of focus (Koch *et al.*, 1998), one can obtain a defect of focus of $z = 36$ μm and $z_{\rm highest} = 64$ μm for a resolution of 5 μm which is twice the effective pixel size of 2.5 μm in the case of a 90% integrated line-spread function. From the above calculations, the optimal thickness of the scintillator is between 36 and 64 μm.

Before the development of the high-efficiency lenses system was completed, in order to find out the optimal scintillator thickness for the system, we used an existing 10× (NA = 0.4) lenses system to evaluate the image contrast because its NA is close to that of the 8× system (NA = 0.5) to be developed. The imaging quality of the detector with different scintillator thicknesses of 50, 100, 130 and 200 μm was compared using the JIMA RT RC-02 test pattern (JIMA, Japan).

Fig. 4 shows the influence of the scintillator thickness on the contrast with the 10× lenses system. As shown, the contrast improves with increasing thickness of the scintillator until the defect of focus is reached, and then degrades. For the best contrast with the 10× lenses system, the optimal scintillator thickness is 50 μm. As shown in Fig. 4, contrast was obtained by using features of 3, 4 and 5 μm in the JIMA RT RC-02 test pattern, and the test result shows that a spatial resolution of 10 μm was reached.

Fig. 5 shows the influence of the scintillator thickness on the contrast of images of sandpaper samples with a 10× lenses system at 18 keV. The imaging quality of the detectors with different scintillator thicknesses of 50, 100, 130 and 200 μm is compared. Four line-profile plots show that the contrast is 0.64, 0.48, 0.27 and 0.18 for scintillator thicknesses of 50, 100, 130 and 200 μm, respectively. The image obtained with the scintillator thickness of 50 μm shows the best quality and the highest contrast for the 10× lenses system. Therefore, the 50 μm-thick scintillator matches the 8× (NA = 0.5) lenses system of the fast X-ray imaging detector to be developed. A 100 nm-thick aluminium reflection layer is coated on the scintillator incident surface and a 100 nm-thick anti-reflection layer is coated on the scintillator exit surface to further improve the detector efficiency. The scintillators were bought from CRYTUR (Turnov, Czech Republic).

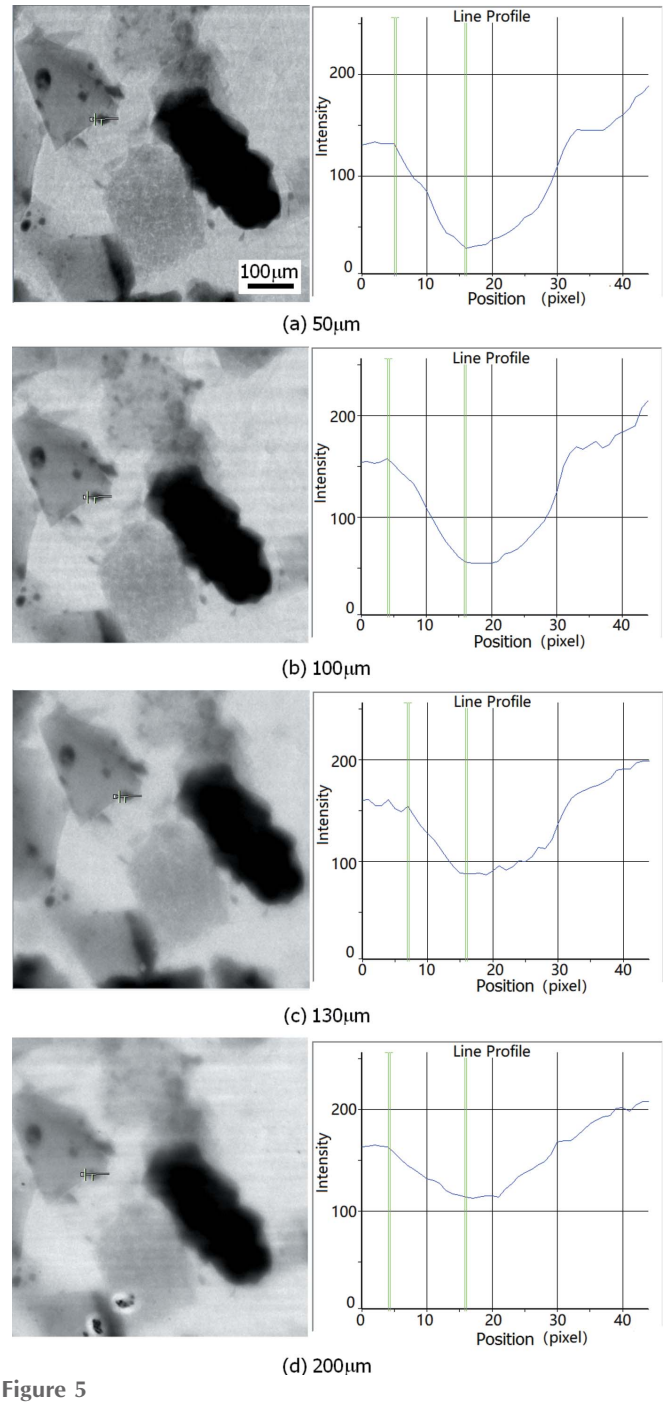

Figure 5
The influence of the scintillator thickness on the contrast of images of sandpaper samples with a 10× lenses system at 18 keV.

5. Performance test

5.1. Scintillator performance test

On the X-ray imaging beamline (BL13W) at SSRF, the imaging performance of the developed fast X-ray imaging detector with four different kinds of scintillators was compared using monochromatic beams of different energy. The scintillators were a 50 μm-thick coated YAG:Ce scintillator, a 50 μm-thick uncoated YAG:Ce scintillator, a 50 μm-thick coated LuAG:Ce scintillator and a 50 μm-thick uncoated LuAG:Ce scintillator. These coated scintillators had a layer of 100 nm-thick aluminium reflection coating on the scintillator incident surface and a layer of 100 nm-thick anti-reflection coating on the scintillator exit surface. The scintillators were bought from CRYTUR (Turnov, Czech Republic).

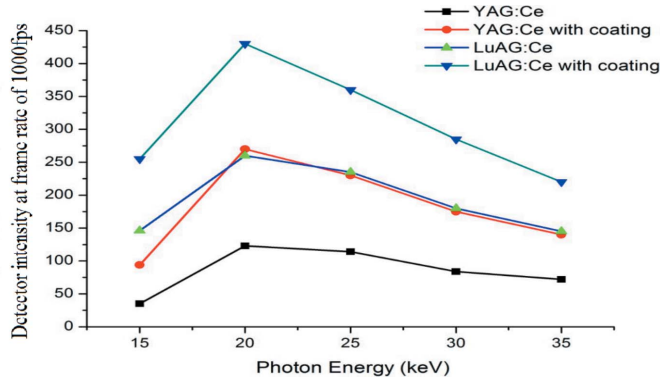

Figure 6
Comparison of detector intensity obtained by the developed detector with the four different scintillator types.

The test results are shown in Fig. 6. From Fig. 6 it can be seen that, in the case of monochromatic beam and a spatial resolution of 10 μm, the developed fast X-ray imaging detector with the four kinds of scintillators can realize a frame rate of 1000 frames s^{-1} within the energy range 15–35 keV, which is used frequently in experiments. It can also be seen from the figure that the intensity of the detector with the coated LuAG:Ce scintillator is the highest compared with the other three kinds of scintillators. The intensity of the detector with the coated LuAG:Ce scintillator is three times that obtained by the detector with the uncoated YAG:Ce scintillator.

According to the signal-to-noise ratio (SNR) equation for optically coupled X-ray imaging detectors (Liu *et al.*, 1996), we can also evaluate electron numbers on the detector generated by a single X-ray photon. The light yield of YAG:Ce is 24000 photons MeV^{-1} (Nikl, 2006; Chewpraditkul *et al.*, 2009) and the light yield of LuAG:Ce is 27000 photons MeV^{-1} (Chewpraditkul *et al.*, 2009; Mares *et al.*, 2012). The energy-conversion efficiency η of 50 μm-thick YAG:Ce and 50 μm-thick LuAG:Ce at 20 keV is 0.5 and 0.7, respectively. At 20 keV, we obtained the X-ray to light conversion ratio g_1 = 480 for YAG:Ce and g_1 = 540 for LuAG:Ce. The optical coupling efficiency of the large NA lenses g_2 = 0.15 at the transmission efficiency τ = 0.9 of optical photons through all the glass lenses. The quantum efficiency of the CMOS g_3 = 0.4 at a wavelength of 550 nm. We also obtained the total quantum gain $\eta g_1 g_2 g_3 = 0.5 \times 480 \times 0.15 \times 0.4 = 14$ electrons per X-ray photon for YAG:Ce and $\eta g_1 g_2 g_3 = 0.7 \times 540 \times 0.15 \times 0.4 = 22$ electrons per X-ray photon for LuAG:Ce at 20 keV, respectively.

5.2. Performance test of image acquisition rate

Some test experiments were performed with the developed detector on the test beamline (BL09B) at SSRF. Fig. 7 shows

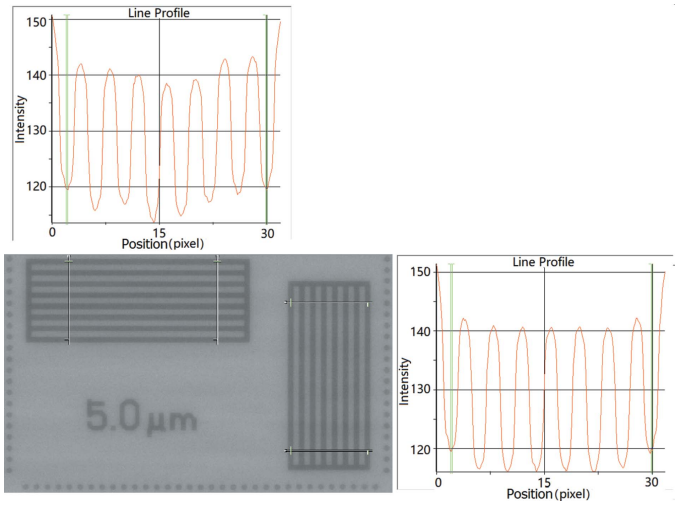

Figure 7
Spatial resolution test result at an imaging frame rate of 100000 frames s^{-1} with the test pattern.

the test result of fast X-ray imaging with spatial resolution of 10 μm at a frame rate of 100000 frames s^{-1} has been reached.

Fig. 8 shows images of the stretching process of the leg of a living grasshopper obtained at a frame rate of 100000 frames s^{-1} using the developed detector, where the whole process of the grasshopper's leg stretching has been clearly recorded. The whole motion process takes about 40 ms, with an inter-frame time of 10 μs and a spatial resolution of 10 μm. The field of view is 1.6 mm by 0.7 mm. We can clearly see the structure detail including tiny tibia bristle and the hamstring tendon of the grasshopper's tibia during the stretching process. This indicates that the developed fast X-ray imaging detector can obtain phase-contrast images for speeds as high as 100000 frames s^{-1}.

A fast micro-CT experiment was performed with the developed fast X-ray imaging detector. The sample was a living ant held in a plastic tube. Fig. 9 shows a series of reconstructed 3D images of the moving process of the legs of the ant by use of dynamic micro-CT at a frame rate of

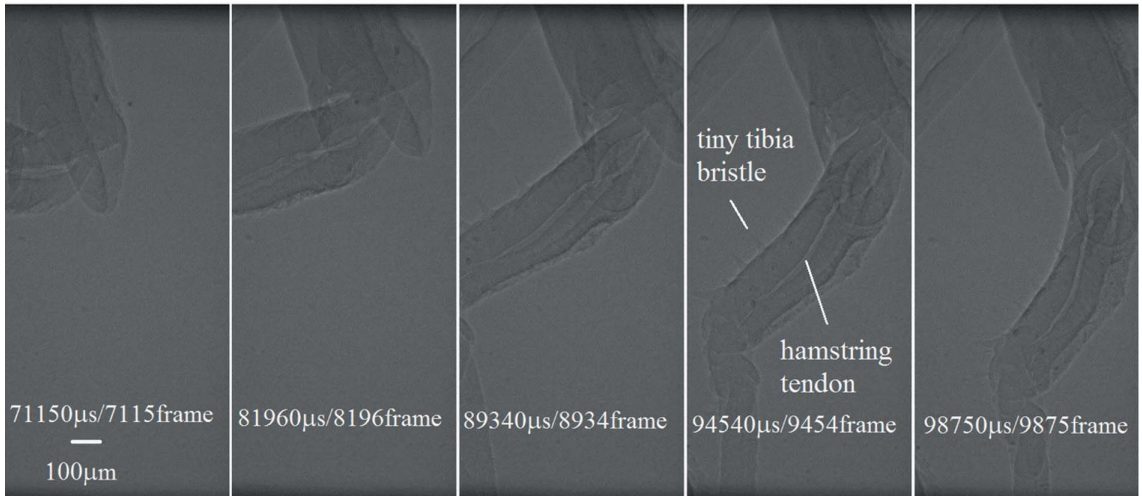

Figure 8
Series of images of the stretching process of the leg of a living grasshopper obtained using the developed detector at a frame rate of 100000 frames s^{-1}.

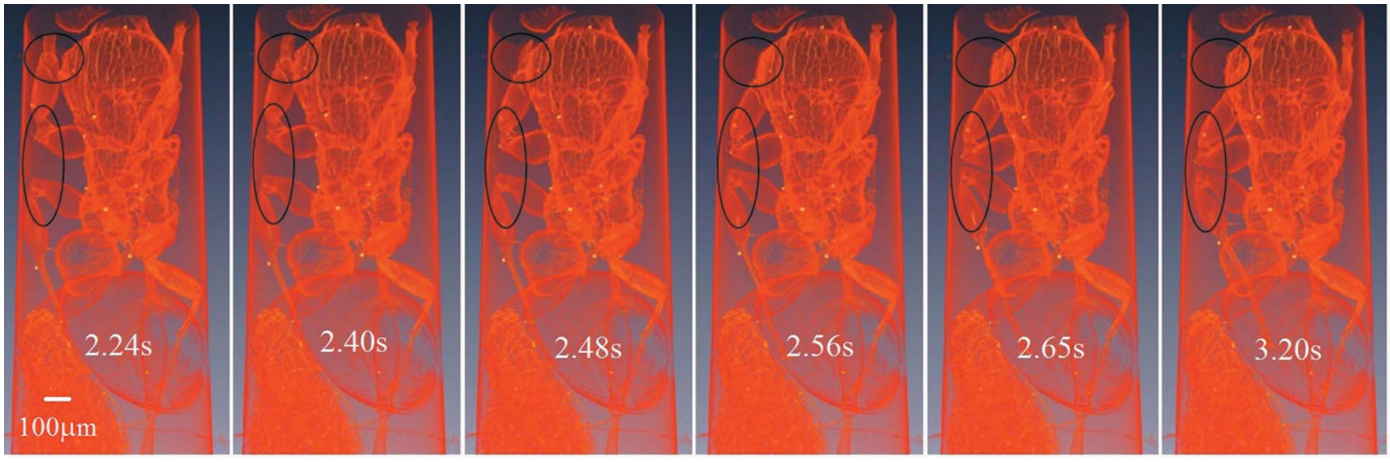

Figure 9
Series of reconstructed 3D images of the moving process of the body of a living ant by dynamic micro-CT using the developed detector at a frame rate of 8000 frames s^{-1}.

8000 frames s^{-1}. The lower-left part of each image is an image of a paper ball which was used to fix the body of the ant in the plastic tube. The 3D reconstruction of each micro-CT used 320 projections. Therefore, the temporal sampling rate of the dynamic micro-CT experiment is 25 Hz. From Fig. 9, we can see the fine structure of the body of the ant including the abdomen, tail and four legs. The black ovals mark the positions of movement of the legs. The experimental results show that the movement of the legs takes 0.96 s and the maximum displacement is about 50 µm (see the supporting information for an example video of the moving process of the ant).

6. Conclusions

A fast X-ray imaging detector based on a long-working-distance optical coupling system has been reported. By optimizing the optical design of the coupling system, the NA of the optical coupling system increased to about two times that of the Mitutoyo long-working-distance lenses.

The performance of the key scintillator materials in the detector was studied. The scintillator with thickness matched with the microlenses NA is used to improve the imaging contrast. The 50 µm-thick LuAG scintillators with 100 nm aluminium reflection film deposited on the incident surface and anti-reflective film on the ejection surface were chosen to be used.

In this way, the efficiency of the detector was noticeably increased. The test results showed that the detector realized fast X-ray imaging with a temporal resolution of 10 µs and a spatial resolution of 10 µm. Fast X-ray imaging of a living grasshopper was performed with the developed detector. The whole process of the grasshopper's leg extension was recorded at a frame rate of 100000 frames s^{-1}. Detailed structures of the leg can be clearly seen, indicating that the detector can obtain high-contrast images at a high speed of 100000 frames s^{-1}. Moreover, a fast micro-CT experiment with a temporal sampling rate of 25 Hz and a spatial resolution of 10 µm was performed. The developed high-efficiency fast X-ray imaging detector will help SSRF users to observe fast processes and the 3D microstructure evolution of materials.

Funding information

This work is supported by the National Key Research and Development Program of China (Grant No. 2017YFA0403801 and Grant No. 2016YFA0401302), and the National Major Scientific Instruments and Equipments Development Project of China (Grant No. 11627901).

References

Bonse, U. & Busch, F. (1996). *Prog. Biophys. Mol. Biol.* **65**, 133–169.
Chen, R., Liu, P., Xiao, T. & Xu, L. X. (2014). *Adv. Mater.* **26**, 7688–7691.
Chen, W. W., Hudspeth, M. C., Claus, B., Parab, N. D., Black, J. T., Fezzaa, K. & Luo, S. N. (2014). *Philos. Trans. R. Soc. A*, **372**, 20130191.
Chewpraditkul, W., Swiderski, L., Moszynski, M., Szczesniak, T., Syntfeld-Kazuch, A., Wanarak, C. & Limsuwan, P. (2009). *Phys. Status Solidi A*, **206**, 2599–2605.
Douissard, P. A., Cecilia, A., Rochet, X., Chapel, X., Martin, T., Kamp, T., Helfen, L., Baumbach, T., Luquot, L., Xiao, X., Meinhardt, J. & Rack, A. (2012). *J. Instrum.* **7**, P09016.
Fan, D., Lu, L., Li, B., Qi, M. L., E, J. C., Zhao, F., Sun, T., Fezzaa, K., Chen, W. & Luo, S. N. (2014). *Rev. Sci. Instrum.* **85**, 113902.
Fezzaa, K. & Wang, Y. (2008). *Phys. Rev. Lett.* **100**, 104501.
García-Moreno, F., Kamm, P. H., Neu, T. R. & Banhart, J. (2018). *J. Synchrotron Rad.* **25**, 1505–1508.
Halls, B. R., Radke, C. D., Reuter, B. J., Kastengren, A. L., Gord, J. R. & Meyer, T. R. (2017). *Opt. Express*, **25**, 1605–1617.
Huang, J. Y., Lu, L., Fan, D., Sun, T., Fezzaa, K., Xu, S. L., Zhu, M. H. & Luo, S. N. (2016). *Scr. Mater.* **111**, 114–118.
Hudspeth, M., Claus, B., Dubelman, S., Black, J., Mondal, A., Parab, N., Funnell, C., Hai, F., Qi, M. L., Fezzaa, K., Luo, S. N. & Chen, W. (2013). *Rev. Sci. Instrum.* **84**, 0251027.
Hudspeth, M., Sun, T., Parab, N., Guo, Z., Fezzaa, K., Luo, S. & Chen, W. (2015). *J. Synchrotron Rad.* **22**, 49–58.
Koch, A. (1994). *Nucl. Instrum. Methods Phys. Res. A*, **348**, 654–658.
Koch, A., Raven, C., Spanne, P. & Snigirev, A. (1998). *J. Opt. Soc. Am. A*, **15**, 1940.
Lee, J. S., Weon, B. M., Je, J. H. & Fezzaa, K. (2012). *Phys. Rev. Lett.* **109**, 204501.
Liu, H., Fajardo, L. L. & Penny, B. C. (1996). *Acad. Radiol.* **3**, 799–805.
Luo, S. N., Jensen, B. J., Hooks, D. E., Fezzaa, K., Ramos, K. J., Yeager, J. D., Kwiatkowski, K. & Shimada, T. (2012). *Rev. Sci. Instrum.* **83**, 073903.
MacPhee, A. G., Tate, M. W., Powell, C. F., Yue, Y., Renzi, M. J., Ercan, A., Narayanan, S., Fontes, E., Walther, J., Schaller, J., Gruner, S. M. & Wang, J. (2002). *Science*, **295**, 1261–1263.
Manin, J., Skeen, S. A. & Pickett, L. M. (2018). *Opt. Eng.* **57**, 124105.
Mares, J. A., Nikl, M., Beitlerova, A., Horodysky, P., Blazek, K., Bartos, K. & D'Ambrosio, C. (2012). *IEEE Trans. Nucl. Sci.* **59**, 2120–2125.
Nikl, M. (2006). *Meas. Sci. Technol.* **17**, R37–R54.
Olbinado, M. P., Cantelli, V., Mathon, O., Pascarelli, S., Grenzer, J., Pelka, A., Roedel, M., Prencipe, I., Garcia, A. L., Helbig, U., Kraus, D., Schramm, U., Cowan, T., Scheel, M., Pradel, P., De Resseguier, T. & Rack, A. (2018). *J. Phys. D Appl. Phys.* **51**, 055601.
Olbinado, M. P., Grenzer, J., Pradel, P., Resseguier, T. D., Vagovic, P., Zdora, M.-C., Guzenko, V. A., David, C. & Rack, A. (2017*a*). *J. Instrum.* **13**, C04004.
Olbinado, M. P., Just, X., Gelet, J., Lhuissier, P., Scheel, M., Vagovic, P., Sato, T., Graceffa, R., Schulz, J., Mancuso, A., Morse, J. & Rack, A. (2017*b*). *Opt. Express*, **25**, 13857–13871.
Rack, A., Garcia-Moreno, F., Schmitt, C., Betz, O., Cecilia, A., Ershov, A., Rack, T., Banhart, J. & Zabler, S. (2010). *J. X-ray Sci. Technol.* **18**, 429–441.
Rutherford, M. E., Chapman, D. J., White, T. G., Drakopoulos, M., Rack, A. & Eakins, D. E. (2016). *J. Synchrotron Rad.* **23**, 685–693.
Wang, J. (2005). *J. Synchrotron Rad.* **12**, 197–207.
Wang, Y. J., Liu, X., Im, K., Lee, W., Wang, J., Fezzaa, K., Hung, D. L. S. & Winkelman, J. R. (2008). *Nat. Phys.* **4**, 305–309.
Xie, H., Deng, B., Du, G., Fu, Y., He, Y., Guo, H., Peng, G., Xue, Y., Zhou, G., Ren, Y., Wang, Y., Chen, R., Tong, Y. & Xiao, T. (2013). *J. Instrum.* **8**, C08003.
Xie, H., Du, G., Deng, B., Chen, R. & Xiao, T. (2016). *J. Instrum.* **11**, C03057.
Yeom, J.-Y., Roh, Y.-J., Jung, C.-O. & Jeong, D.-H. (2010). *Int. J. Optomechatron.* **4**, 34–50.
Zhou, T., Wang, H., Connolley, T., Scott, S., Baker, N. & Sawhney, K. (2018). *J. Synchrotron Rad.* **25**, 801–807.